Plastic deformation of minerals at high pressure: Multiscale numerical modelling

Patrick Cordier, Fabrice Barbe, Julien Durinck, Andrea Tommasi, Andrew Walker

EMU Notes in Mineralogy, Vol. 7 (2005), Chapter 16, 389–415

Plastic deformation of minerals at high pressure: Multiscale numerical modelling

PATRICK CORDIER[1]*, FABRICE BARBE[2], JULIEN DURINCK[1], ANDREA TOMMASI[3] and ANDREW M. WALKER[4†]

[1]*Laboratoire de Structure et Propriétés de l'Etat Solide, UMR CNRS 8008, Université des Sciences et Technologies de Lille, 59655 Villeneuve d'Ascq Cedex, France*
[2]*Laboratoire de Mécanique de Rouen, EA 2838, INSA Rouen, BP8, 76800 Saint-Etienne du Rouvray, France*
[3]*Laboratoire de Tectonophysique, UMR CNRS 5568, Université Montpellier II, France*
[4]*Davy Faraday Research Laboratory, The Royal Institution of Great Britain, 21 Albemarle Street, London, W1S 4BS, UK;*
†*Present address: Research School of Earth Sciences, The Australian National University Mills Road, Canberra, ACT 0200, Australia*
**e-mail: Patrick.Cordier@univ-lille1.fr*

Introduction

Multiscale modelling and computation is becoming one of the most active research areas in materials science. This evolution is driven by the rapid growth in available computing power and by the development of many innovative algorithms and techniques. In mineral physics, the issue of mantle rheology, controlled by the deformation of high-pressure mineral assemblages, can be addressed by this new approach. In contrast with thermodynamic properties like the equation of state, which are fully determined at the atomic length scale, mechanical properties are inherently multiscale: they depend on the interrelationship between processes operating at the scale of the atom, the crystal, the rock and the whole planet. Moreover, these different scales are often strongly coupled to each other, which makes the problem even more challenging.

From the atoms to the Earth's mantle

Mechanical properties of real materials are controlled by crystal defects such as point defects, dislocations, stacking faults and grain boundaries. Taken individually, these defects can be described at the fundamental level through their atomic and electronic structures, which can be found by solving the Schrödinger equation. First-principles calculations and molecular dynamics are used to address such problems. At the scale of a grain, the mechanical properties are often the result of the collective behaviour of these defects in response to the loading conditions. Newly developed three-dimensional dislocation dyna-

mics simulation techniques are aimed to take these interactions between defects into account to provide insights about single-crystal plasticity. Constitutive laws for single-crystal plasticity can be ultimately transferred to the scale of the polycrystal. Polycrystal plasticity models and finite-element methods based on continuum mechanics examine how an aggregate (with possibly several phases) will deform in response to an applied stress. It is here necessary to describe, for a given microstructure, how stress and strain are partitioned between the various grains. The ultimate goal is to derive macroscopic constitutive relations that can be used into large-scale mantle convection models (Fig. 1). It is to be noted that this final step involves not only a large extrapolation in length scales, but also in time scales as mantle convection takes place over very long times. The main purpose of the present chapter is to illustrate some of the ongoing efforts for setting the basis of multiscale modelling of plastic deformation of mantle minerals.

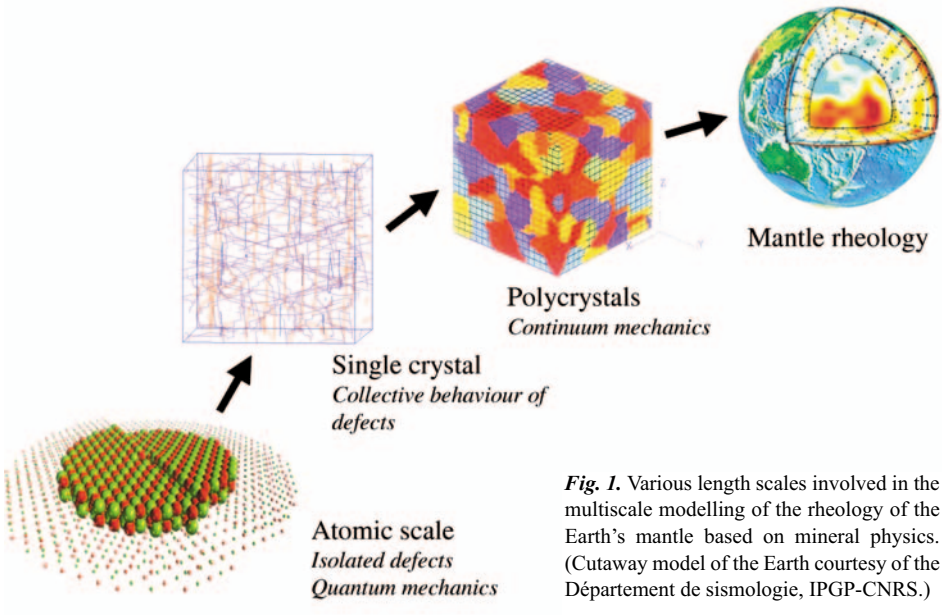

Fig. 1. Various length scales involved in the multiscale modelling of the rheology of the Earth's mantle based on mineral physics. (Cutaway model of the Earth courtesy of the Département de sismologie, IPGP-CNRS.)

Atomic scale: From atoms to individual defects

Atomistic simulations of the microstructural evolution of defects are clearly central to the understanding of mechanical properties. Several developments in the recent past have made the atomistic approach increasingly attractive. The rapid increase in efficiency and power of computers, coupled with methodological advances allow reasonably sized systems to be studied using common PCs whereas supercomputers have allowed quantum mechanics-based studies of larger systems. Currently, standard techniques using density functional theory (DFT) are limited to hundreds of atoms but research in linear scaling algorithms (recently reviewed by Craig *et al.*, 2004) are beginning to open the way towards DFT studies of millions of atoms. Larger systems can be studied by simplifying

the model, at the expense of predictive accuracy. There are many atomic-scale methods available to study point and planar defects in mantle minerals (for examples of studies of defects in forsterite see Brodholt, 1997; Braithwaite *et al.*, 2003; de Leeuw *et al.*, 2000; and Walker *et al.*, 2003) but here we concentrate on the study of dislocations. Most applications of these techniques for dislocation modelling have been concerned with simple metallic systems and semiconductors. Minerals usually represent a more complicated case because of their large unit cells, low symmetries and complex crystal chemistries. This complexity makes the atomistic approach even more relevant, as such fundamental issues as plastic shear anisotropy (which is responsible for crystal preferred orientations), dislocation mobilities and Peierls stresses need to be addressed at this scale.

Generalised stacking faults and plastic shear anisotropy

A generalised stacking fault (GSF) γ is produced when a crystal is sheared in a given plane by a given displacement u (Vitek, 1968). In general a GSF is not stable and must be balanced by a restoring force $f(u) = -d\gamma/du$. The elementary shears induced in forming a GSF are also found in dislocation cores (Fig. 2). Suppose we consider a dislocation to be spread out in the x–z plane with the dislocation line along the z axis, and the displacement u oriented parallel to the Burgers vector **b**. The dislocation is represented by a continuous distribution of shear across the glide plane given by the density of a continuous distribution $\rho(x) = du/dx$. Normalised to the magnitude of the Burgers vector,

$$\int_{-\infty}^{+\infty} \rho(x)dx = b, \tag{1}$$

the solution arises from a balance between the stress induced by $\rho(x)$ and the restoring force

$$A\int_{-\infty}^{+\infty} \frac{\rho(x')}{x - x'}dx' = -\frac{d\gamma(u)}{du}. \tag{2}$$

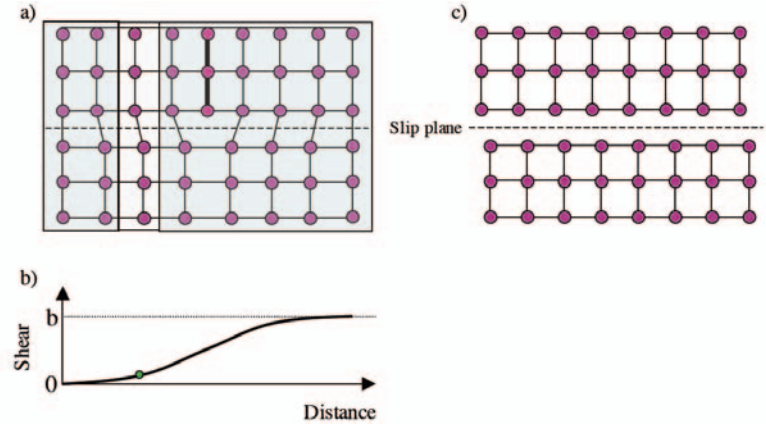

Fig. 2. (a) Schematic representation of an edge dislocation. ***(b)*** Distribution of shear along the slip plane in the vicinity of the dislocation core. At a given distance (as the one highlighted in *(a)*) corresponds a given elementary shear value. ***(c)*** The GSF corresponding to this elementary shear can be calculated by imposing it homogeneously across the slip plane.

The GSF are thus intimately related to the dislocations although they are much easer to study. They provide, through their derivative the restoring force, information about glide plane corrugation at the atomic scale. This information tells us the ease or difficulty of shearing a crystal structure in a particular direction in a given plane, providing an upper bound for the shear strength, but also information about shear anisotropy.

Here we present some preliminary results obtained from a study of forsterite (Mg_2SiO_4). The calculations of the GSF excess energies are done in the following way[1]. First, a stacking plane is chosen, here we present results concerning (100), (010), (001), (110) and (021) planes. The height of the fault plane is chosen to preserve the structural SiO_4 tetrahedron. For a given stacking plane, two lattice translations in the plane perpendicular to each other are chosen as principal directions for the supercell used to model the GSF. The third supercell direction is chosen perpendicular to the GSF plane. Since forsterite does not have cubic symmetry, this third direction may not be a lattice translation, which implies that when periodic lattice conditions are applied, the upper and lower parts of the supercell are not necessarily commensurate. To avoid this difficulty, and in order to calculate GSF excess energies for any fault vector **u** (see below), a 6 Å thick vacuum buffer is added to the stacking of atomic planes perpendicular to the fault. Once the supercell is built, the upper part of the supercell is moved with respect to the lower part by **u**, the fault vector contained in the fault plane (see Fig. 3). Once the translation is made, the atoms are allowed to relax and the energy of the system is calculated providing the excess energy associated with the fault. The energy barrier associated with [001](110) shear is presented Figure 3b, where the three sheared configurations shown on Figure 3a are emphasised. Figure 4 summarises the results of calculations performed for several potential slip systems in olivine. The various slip systems can be sorted, based on the GSF excess energy, into the following categories:

– easy: [001] glide (Fig. 4a), especially on the (010) plane;
– intermediate: [100] glide (Fig. 4b) with (021) appearing as the easiest plane;
– difficult: [010] glide brings atoms in very unfavourable positions during shear leading to very high (and physically meaningless) stacking fault energies (not presented).

This picture is consistent with the low-temperature plasticity of forsterite. First-principles calculations of GSF provide a rational picture for the anisotropy of plastic shear of forsterite in connection with the crystal chemistry. In spite of its simplicity, the GSF concept is extremely relevant to decipher the influence of the crystal chemistry on plastic shear.

A major advantage of *ab initio* calculations is that, being based on a strong physical basis, they can be applied under various conditions including high pressures. The same GSF have been calculated plastic shear in forsterite at 10 GPa. The results are presented Figures 4c and d for [001] and [100] slip on (010). It appears that [001](010) is only slightly affected

[1] The calculations have been performed using the *ab initio* total-energy calculation package VASP (Vienna Abinitio Simulation Program) developed at the Institut für Materialphysik of the Universität Wien (Kresse & Hafner, 1993; Kresse & Furthmüller, 1996a, 1996b). This code is based on the first-principles density functional theory and solves the effective one-electron Hamiltonian involving a functional of the electron density to describe the exchange–correlation interaction. (Strictly speaking the expression "atomic scale" is not appropriate as calculations are performed at the electronic scale.) It gives access to the total energy of a periodic system without any experimental input but the atomic numbers of the atoms.

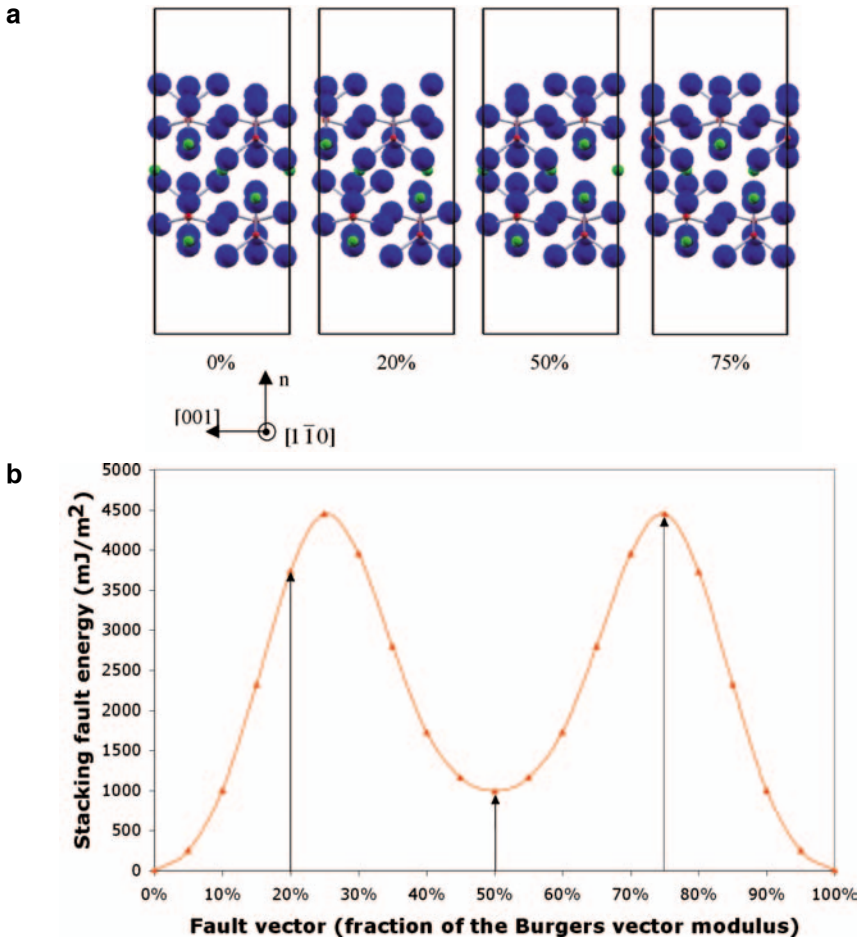

Fig. 3. Generalised stacking faults. ***(a)*** Supercell used to investigate plastic glide resistance in forsterite along [001] on (110). The unsheared supercell is presented on the left whereas three shear stages (20%, 50 % and 75% of the [001] lattice vector) are presented on the right side. ***(b)*** Energy barrier associated with [001](110) plastic shear.

by pressure. Only the shape of the barrier (which is not discussed here) is modified. In contrast, the barrier for [100](010) is significantly increased under pressure. The analysis of atomic relaxations shows that [100] glide involve dilations that inhibit glide at high pressure. This calculation provides a theoretical frame to account for dominant [001] glide at high pressure in forsterite deformed in the multi-anvil apparatus (Couvy *et al.*, 2004).

Dislocation modelling

The GSF approach attempts to determine the plastic properties of a mineral from just the crystal structure and chemistry, which are specific properties of its unit cell; moving up in scale one can model the core of an isolated dislocation at the atomic scale. Such models require many more atoms to be simulated (depending on the crystal structure, perhaps a

few tens or hundreds are needed to study the GSF but tens to hundreds of thousands are needed to study isolated dislocations), which requires a change in methodology from a first-principles DFT approach to a method based on parameterised interatomic potentials. This in turn implies some loss of predictive power as the correct treatment of the electronic structure of the mineral is discarded in favour of a simpler and less computationally intensive procedure. Even so, simulation of a hundred thousand atoms using parameterised potentials is not a trivial calculation, it requires substantial CPU time and special algorithms for the treatment of, for example, the Columbic interactions.

The approach described here is to model a single, straight dislocation in an otherwise defect-free infinite crystal (*e.g.* Hoagland *et al.*, 1976; Puls & Norgett, 1976; Watson *et al.*, 1999). This avoids potential difficulties with dislocation–dislocation interactions implicated in supercell approaches common in studies of semi-conductors (*e.g.* Bigger *et al.*, 1992; Cai *et al.*, 2001; Martsinovich *et al.*, 2003; see Fig. 5). Away from the dislocation core the crystal is described as an elastic continuum while the core and its immediate surroundings are composed of discrete atoms. The interface between the continuum and atomistic regions consists of model atoms fixed in locations predicted by linear elasticity. These atoms may be fixed for the duration of the calculation (fixed boundary conditions: Hoagland *et al.*, 1976; Watson *et al.*, 1999; Marian *et al.*, 2004; Walker *et al.*, 2004) or may move (flexible boundary conditions: Gehlen *et al.*, 1972; Sinclair *et al.*, 1978; Rao *et al.*, 1998).

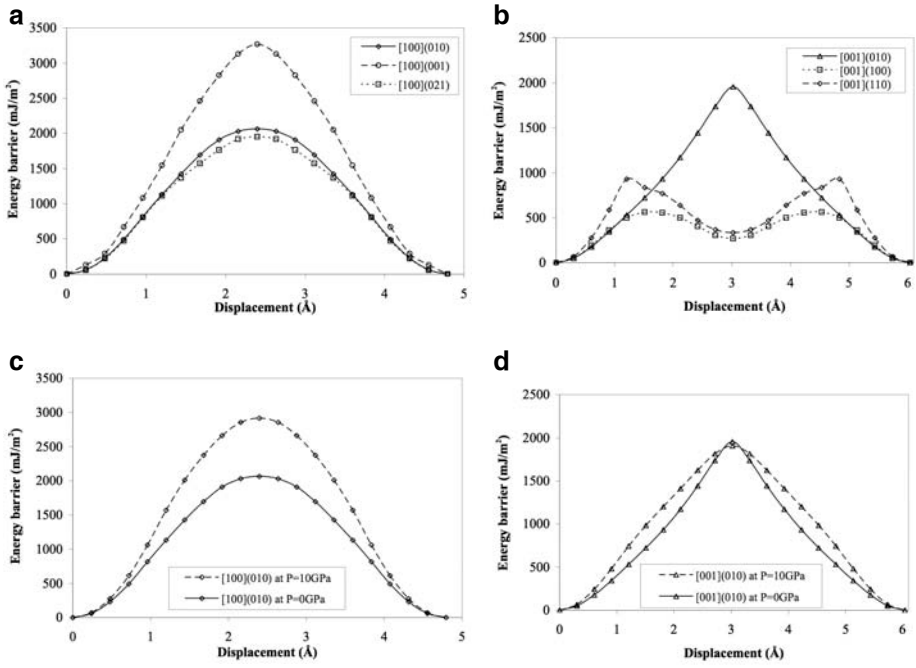

Fig. 4. Generalised stacking faults in forsterite. ***(a)*** [100] slip systems at $P = 0$ GPa. ***(b)*** [001] slip systems at $P = 0$ GPa. ***(c)*** Influence of pressure on the [100](010) slip system. ***(d)*** Influence of pressure on the [001](010) slip system.

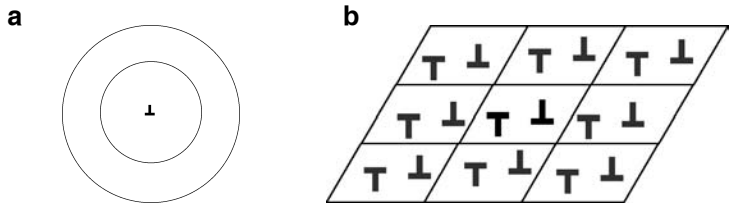

Fig. 5. Two ways to construct a model of a dislocation core at the atomic scale, looking along the dislocation line. ***(a)*** Isolated dislocation methodology used here with the inner region relaxed and the outer region treated as an elastic continuum with the interface region marked. ***(b)*** Setup for a supercell calculation; note that the problem of cancelling the elastic interaction between images of the dislocation has been solved (Cai *et al.*, 2001) but Coulombic interactions between the atoms around the dislocations are harder to deal with when the atoms have net charge.

In practice, the modelling is performed as follows. First, the potential model is used to calculate the structure and elastic constants of the perfect infinite crystal. Second, a disk-shaped model is created which is centred on the intended location of the dislocation line and is periodic in the direction of the line. Third, using the calculated elastic constants the displacement field associated with the dislocation is calculated at the location of each atom in the model and the displacement is applied – this has the effect of introducing the dislocation. Fourth, energy minimisation is performed to the model with some of the atoms close to the edge of the cell held fixed (or being periodically moved according to the forces on them and the rules of a flexible boundary condition). This process yields the structure of the core of the dislocation; this can be used to extract the energy of the dislocation core and its displacement, stress and strain fields.

As a simple example we present results of modelling an **a**{100} screw dislocation in MgO[2]. Introduction of the dislocation is relatively straightforward in this case as the anisotropic displacement field reduces to the isotropic form (Steeds, 1973):

$$u_x = 0;$$
$$u_y = 0;$$
$$u_z = \frac{b}{2\pi} \arctan \frac{y}{x}.$$

As well as defining its form, an origin for the displacement field must be selected. There are three obvious possibilities for the location of the origin of the displacement field termed the edge, ion and centre sites, as shown in Figure 6 (Watson *et al.*, 1999).

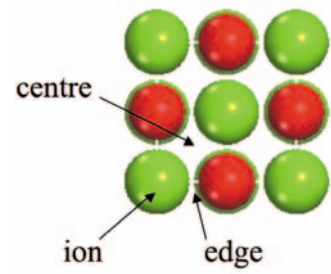

Fig. 6. Three locations used to centre the 1D simulation cell and the elastic displacement field for models of the ⟨100⟩ screw dislocation in MgO.

[2] The breathing shell model of Gale & Rohl (2003) is used as this gives a good representation of the elastic properties of MgO. Convergence testing was carried out in order to select sizes for the relaxed (Region 1) and fixed regions (Region 2) in the calculation; these showed Region 1 should have a radius of 50 Å and the radius of Region 2 should have a thickness of 15 Å. All the cells were one unit cell thick. Energy minimisation was performed using the conjugate gradients method and the Coulomb summation of Saunders *et al.* (1994) implemented within the latest version of the GULP code (Gale & Rohl, 2003).

The cells centred on these three sites contained 8994, 8943 and 9000 species (Mg cores, O cores and O shells), respectively.

Figure 7 shows the final structure of the core of the [100] screw dislocation (all three cells give essentially the same geometry). In analysing this structure, it is useful to compare the final structure with the starting structure as derived by linear elastic theory; Figure 8 shows this difference, which is termed the core displacement field. The core relaxation can conveniently be separated into two parts with distinct causes. The first effect is that the atoms tend to move in towards the core (Fig. 8a). This mode of displacement is because a group of atoms, which originally formed a circle around the incipient dislocation line, forms a helix after the introduction of the dislocation. As the elastic displacement field does not contain components perpendicular to the dislocation line, the radius of the helix and the original circle are the same, so that all the Mg–O bond distances are increased by the process of introducing the dislocation. On relaxation, these bond distances tend to reduce towards their natural values in the bulk, which is achieved by the inwards relaxation. The second mode of displacement is motion parallel to the dislocation line (Fig. 8b). This occurs because of the discontinuity at the origin of the elastic displacement field (for example, an atom at a short distance along the positive x axis has a θ value of 0, a short distance along the negative y axis gives a value of 180 degrees, the displacement along z for these two points are 0 and 0.5 times the Burgers vector, respectively; crossing the origin leads to a step of $0.5b$ in the displacement field). In MgO this discontinuity is equal to the Mg–O separation so that like atoms are brought into contact across the discontinuity. This is clearly energetically unfavourable so the atoms close to the core move along z to remove the discontinuity. It is notable that the total displacement in z is equal to 2.4 ångströms, or half the Burgers vector.

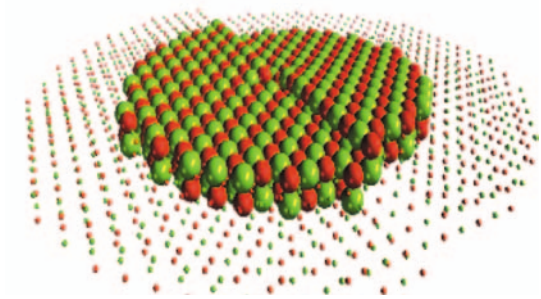

Fig. 7. An atomic model of the [100] screw dislocation in MgO. Mg ions are shown in red and O ions are shown in green. In the inner region, represented by large spheres, the ions are explicitly moved to achieve energy minimum while the ions in the outer region are held fixed at positions predicted by linear elastic theory. The inner region must be large enough to accommodate the relaxation of the core and non-linear contributions to the relaxation.

From the model of the dislocation core, the dislocation formation energy (*i.e.* the reversible work done on the introduction of the dislocation) can be found. This energy, which is just the difference between the energy stored within a defined radius from the dislocation in the model with a dislocation and the equivalent energy in the model without a dislocation, can be separated into two parts, a core contribution and an elastic contribution. The total energy is fitted to the elastic solution to the dislocation energy:

$$E(r) = E(\text{core}) + \frac{K}{4\pi} \ln\left(\frac{r}{r_0}\right), \qquad (3)$$

where $E(r)$ is the energy stored within a radius r, E(core) is the core energy and r_0 is the radius of the core. In isotropic elasticity, K is the shear modulus but in anisotropic elasticity it is a more complex average of key components of the elastic compliance tensor (Steeds, 1973); Figure 9 shows the critical importance of accounting for anisotropy in the fitting procedure. Taking the core radius as 10 Å, using the anisotropic solution for the elastic energy and only fitting to data from radii that exceed the core radius yields core energies of 4.2213, 4.4408 and 4.1916 eV/Å for the edge, centre and ion sites, respectively.

So far, there are very few published computational studies of dislocations in mantle minerals using either the GSF or dislocation modelling approaches. Both methods are under active development with the aim of allowing studies of systems with more complex crystal structures in order to study dislocations in a wide range of minerals. An interesting

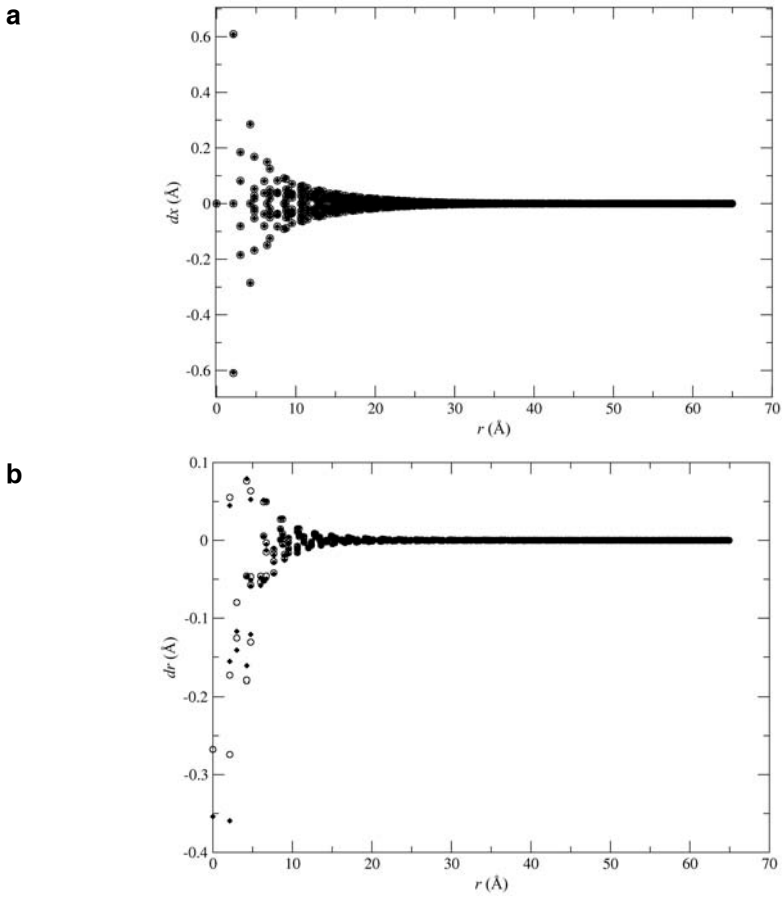

Fig. 8. Relaxation from elastic to atomistic solution for the ⟨100⟩ screw dislocation in MgO (centre site). ***(a)*** Displacements of magnesium ions (black) and oxygen cores (open circles) parallel to the dislocation line smooth out the discontinuity at the origin. ***(b)*** Ionic displacements inwards towards the dislocation line shorten the bond lengths.

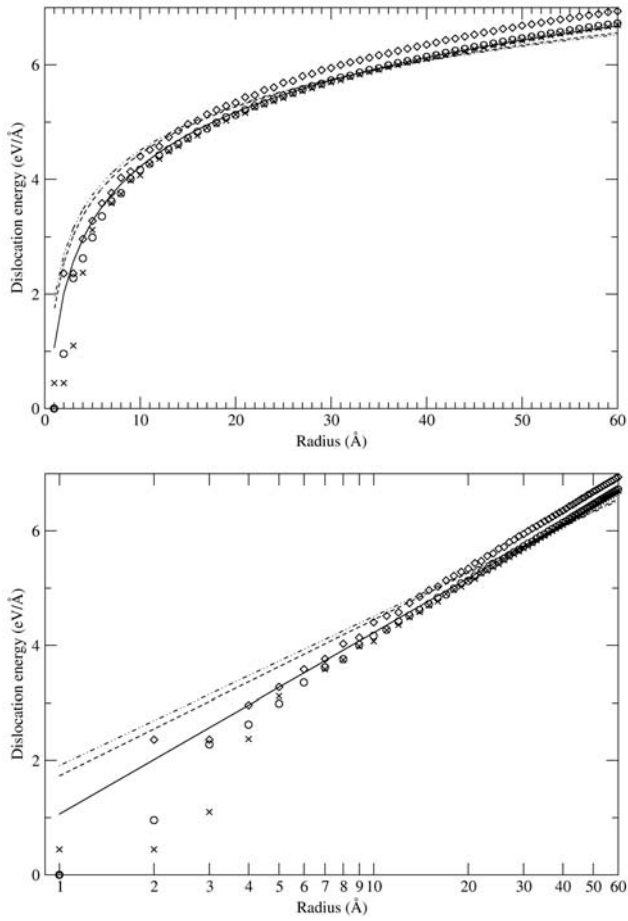

Fig. 9. Energy of MgO screw dislocation. Diamonds, circles and crosses are data taken from the atomistic model for the centre, ion and edge choices of origin. Solid, dashed and dash-and-dot lines are fits to the data for the edge site using the anisotropic, Voigt (133.8 GPa) and Reuss (128.0 GPa) definitions, respectively. The gradient of the line on the log plot clearly shows that the isotropic elastic solution does not fit the results of the atomistic solution but the anisotropic solution does fit the data.

case for dislocation modelling has been zeolite A, where the presence of screw dislocations will radically change its channel system and hence its transport properties. The helical nature of the dislocation core also has potential for enantioselective applications (Walker *et al.*, 2004). An initial attempt to study the structure of dislocations in forsterite and $MgSiO_3$ perovskite, both volumetrically important mantle minerals, has been undertaken and these studies show promise. The GSF and dislocation modelling approaches are complementary in providing information on the atomic scale that is needed as input for calculations on the mesoscopic scale described below. Where the GSF method can give information on plastic anisotropy and an estimate of the Peierls barrier to (idealised) dislocation movement, direct calculation of the structure of the dislocation

core can be used to probe processes such as the formation and migration of kinks and jogs on the dislocation line. All this information is needed as input for the mesoscopic scale models described below, and can only be provided by the interpretation of experimental data or studies on the atomic scale. It is in providing such data that the use of atomic scale methods will be of most use in studies of mantle plasticity.

Mesoscopic scale: Describing dislocation dynamics

The field of mesoscopic simulations, which appeared at the end of the 1980's, is currently evolving very rapidly. These simulations deal with a scale which is intermediate between the atomic scale and the one used in continuum mechanics (which use approaches such as finite-element methods described below). Hence, they are well adapted to describe the plasticity of single crystals or individual grains. In this approach, dislocations are described as individual objects within a continuous medium. The simulated volume must contain enough dislocations to be a representative volume element from the point of view of the mechanical properties. Several codes are available; however, they all share the three main characteristics: discretisation of space, dislocation mobilities and boundary conditions. Based on two different discretisation modes, two main types of 3D simulation can be distinguished. In the first one (Zbib *et al.*, 1998), dislocation lines are discretised with a continuous set of segments with mixed directions, whereas in the second one (Devincre *et al.*, 2001) the dislocation segments are constrained to have a finite number of characters. Results from this second method are described below.

Discretisation of space

A continuous dislocation line is discretised in the form of a succession of edge, screw and mixed segments that are connected together to build up a dislocation line. Eight elementary segments are needed to reproduce a general dislocation loop in a given plane (Madec *et al.*, 2001; see Fig. 10). When a segment moves, the lengths of the two segments

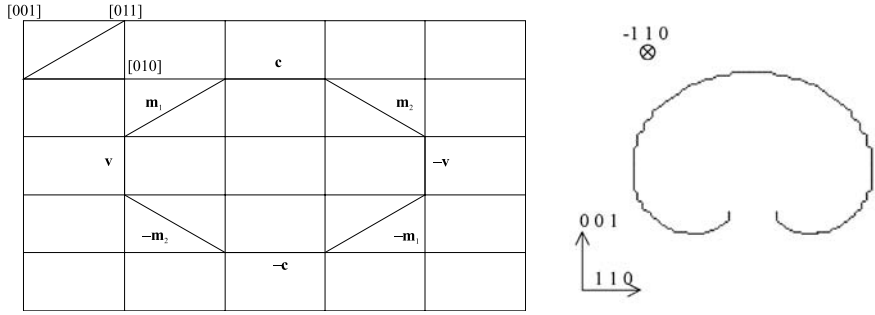

Fig. 10. Dislocation line discretisation. ***(a)*** Example of a dislocation loop in forsterite. Case of the (100)[001] slip system:. Dislocations are discretised as a set of predefined elementary segments ("s" for screw, "e" for edge and "m" for mixed). On the top left are represented the elementary vectors used in the simulation of forsterite and expressed in a cubic lattice of parameter *a*. ***(b)*** Case of a Frank–Read source in MgO (courtesy of Ph. Carrez).

connected to it can be increased to maintain line continuity. These elementary segments are placed on a 3D lattice of nanometric dimension a that exhibits the symmetry of the crystal. This lattice is as small as possible, taking care that the line curvature of dislocations is still well described.

Dislocation mobilities

Dislocations segments create long-range (*i.e.* $\propto 1/r$) stress fields in the surrounding medium. Hence, each point M will bear the stress contribution of every dislocation segment present in the medium. This gives rises to what is called the internal stress σ_{int}. The actual stress state at this point M will be the result of two contributions: the applied stress σ_{app} and the internal stress σ_{int}. The resulting force applied to a given unitary dislocation segment $d\mathbf{l}$ with a Burgers vector $\mathbf{b}$ is given by the Peach–Koehler formula.

$$d\mathrm{F} = \left[\left(\overline{\overline{\sigma_{\text{app}}}} + \overline{\overline{\sigma_{\text{int}}}}\right)\mathbf{b}\right] \times d\mathbf{l}. \tag{4}$$

The effective force acting on a segment is the sum of the Peach–Kohler force and of a local line tension due to the curvature of dislocation (Devincre & Condat, 1992). Responding to this force, the dislocation segment will move perpendicular to its line direction with a velocity v. Note that time has also to be discretised to numerically integrate the Newton equation of motion of the segments. The velocity of the segments is a critical parameter in the simulation. The simplest case is found with fcc metals for which the dislocation mobility results mostly from a dragging force due to the interaction with the phonons:

$$v(\tau) = \tau \frac{b}{B}, \tag{5}$$

where τ is the resolved shear stress, b is the modulus of the Burgers vector and B is the dragging force coefficient. The situation is different for bcc metals for which screw dislocations are found to bear a large lattice friction. The mobility of the dislocations is there due to the nucleation and spreading of kink pairs along the dislocation line. This mechanism is thermally activated. The velocity v of a dislocation segment of length L is given by an Arrhenius rate equation:

$$v = b\frac{L}{l_{\text{c}}}\nu_{\text{D}}\frac{b}{l_{\text{c}}}\exp\left(-\frac{\Delta H(\tau)}{kT}\right), \tag{6}$$

where b is the Burgers vector, ν_{D} is the Debye frequency, l_{c} is the critical length for the kink-pair nucleation, ΔH is the activation enthalpy which is a function of the effective stress τ and kT is the Boltzmann factor. This mobility law depends linearly on the dislocation length L and very strongly on temperature and effective stress through the exponential term. This behaviour is also observed in silicon. Because the strong covalent bonds are the origin of the thermally activated process in that case, every character (edge, screw or mixed) will be affected. Minerals, which usually involve iono-covalent bonding, are likely to follow the same behaviour. For a given time step δt, the dislocation segment will move over a distance $du = v\,\delta t$. It will sweep an area $dA = L\,du$ from which one can calculate the induced shear strain increment $d\gamma = b\,dA/V$ for the volume V containing the dislocation segment. The total shear strain increment will be obtained by

summing the contributions of every dislocation segments. However, it is necessary to check that during its flight, *du*, the segment does not meet any obstacle. In the case of a collision, the interaction with the obstacle will be treated by local rules (junction formation or annihilation for instance).

Boundary conditions

Free-boundary conditions can be used. In that case, a dislocation vanishes when it reaches the surface of the simulation volume. Interactions with the free surfaces might lead to depleted dislocation densities in the vicinity of the free surfaces. Periodic boundary conditions are often used in order to avoid this problem. The simulation volume is then considered as a representative volume element in a much larger crystal. A portion of dislocation loop leaving the simulation volume at a surface re-enters it at a different place (Fig. 11). It is necessary to adjust the position where it re-enters the volume to avoid undesirable effects due to self-interactions (annihilation or dipolar interaction) of portions of dislocation loops with their replicas over the extended simulation volume. The dimensions of the simulation cell have to be adjusted in order to control the self-interaction distance, *d*. A general solution for this problem has been proposed by Madec *et al.* (in press).

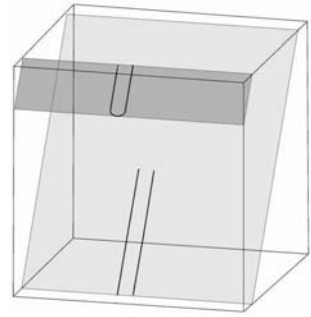

Fig. 11. Anisotropic dislocation loop expanding in its slip plane. When a portion of the loop leaves the simulation cell, it is re-injected inside the cell through periodic boundary conditions.

Application to olivine

The dislocation dynamics simulation is illustrated here in the case of the [001] glide in olivine. The most striking feature of the dislocation microstructures in olivine crystals deformed by [001] glide is the pervasive occurrence of long straight screw segments (Gaboriaud *et al.*, 1981; Gaboriaud, 1986; Phakey *et al.*, 1972; Evans & Goetze, 1979;

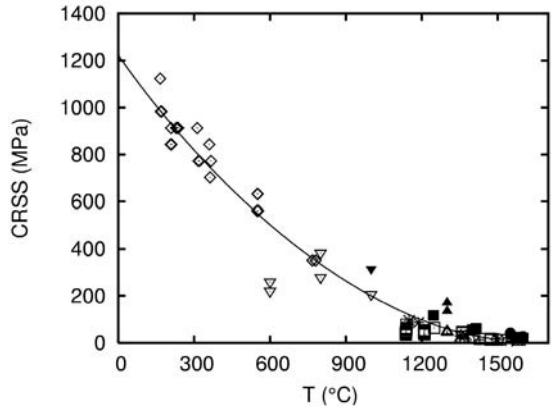

Fig. 12. Critical resolved shear stress (CRSS) for slip systems with [001] Burgers vectors gliding in (010), (100) and {110} planes. The CRSS was determined from deformation experiments performed on olivine single crystals.

Wang *et al.*, 1988; Durham *et al.*, 1977; Gueguen & Darot, 1982; Darot & Gueguen, 1981). This morphology suggests that (i) screw dislocations are facing a high lattice friction, (ii) the mobility of edge segments is high compared to screw segments. As suggested above, we use a thermally activated mobility law to describe the motion of [001] screw segments. Based on a kink-pair mechanism, the mobility law is also dislocation length-dependent. Following the method proposed by Kocks *et al.* (1975) and applied to bcc crystals by Tang *et al.* (1998), the parameters which appear in this law are fitted against experimental mechanical data (Fig. 12). Edge [001] segments move much quickly than screw segments. Given the bonding characteristics of olivine, we have assumed that all segments follow a thermally activated behaviour. The mobilities of the faster segments will simply be chosen to be K times larger than the mobility of the 10 μm long slower ones, at a given stress and temperature. Another important parameter for the simulation is the mean free path λ of the fast segments. In practice, this parameter is determined by the obstacles (subgrain boundaries, grain boundaries, free surfaces *etc.*). These two parameters have been highlighted by Monnet *et al.*, (2004), who showed that they strongly control the amount of pre-yield deformation.

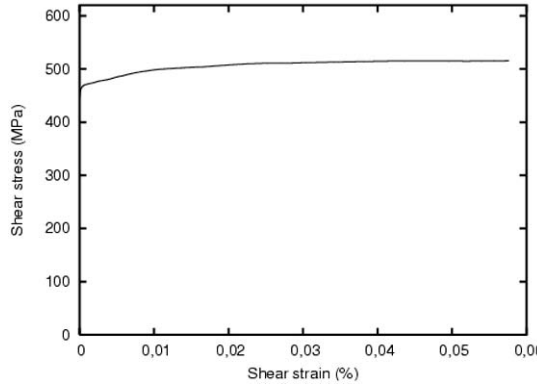

Fig. 13. Stress–strain curve obtained from a numerical experiment corresponding to a [011]*c* orientation at a strain rate of 10^{-5} s^{-1} at 1200 K.

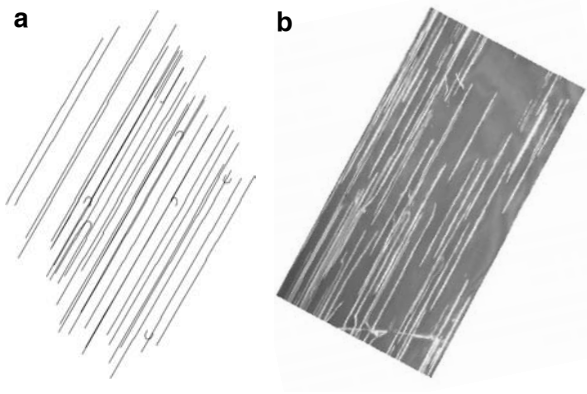

Fig. 14. Comparison between simulated microstructures and their experimental counterparts for forsterite. ***(a)*** DD simulation of a 1 μm-thick thin foil parallel to (010) containing [001] dislocation loops. The temperature of the simulated test is 1200 K. ***(b)*** TEM observation of a forsterite sample deformed at 11 GPa, 1673 K (courtesy of H. Couvy).

We have chosen a factor K of 8000 and a mean free path of 30 μm. These parameter sets give satisfactory dislocation loop aspect ratio and a reasonable pre-yield deformation achieved by the faster non-screw segments. Figures 13 and 14 show the results of numerical deformation experiments (single slip [001](010), with a [011]c stress axis, at 1200 K and at a strain rate of 10^{-5} s^{-1}) performed with this model. They show that the dislocation microstructures are reproduced satisfactorily and that the stress–strain curve is consistent with the critical resolved shear stress for [001](010) (Fig. 12).

From single crystals to polycrystals

Polycrystal plasticity modelling and strain-induced crystal preferred orientations
Polycrystal plasticity models, also known as homogenisation techniques or micro-macro approaches, have been largely used in the last 30 years to predict the evolution of crystal preferred orientations (CPO) of mantle minerals during deformation. These models relate the mechanical behaviour of a polycrystalline aggregate composed by a finite number of crystals, like a mantle sample, to the individual behaviour of its grains. They are composed of two basic equations sets: the first one describes the individual crystals properties and orientations and the second adds the individual crystals mechanical behaviours to define the polycrystal response (Lebensohn *et al.*, 2003).

Single crystal equations are the same for all polycrystal plasticity models. Deformation is homogeneous at the grain scale. It is accommodated by dislocation glide only. The shear rate in a slip system s is related to the local deviatoric stress tensor **s** by a viscoplastic law:

$$\dot{\gamma\gamma}^{s} = \dot{\gamma\gamma}_0 \left(\frac{\tau^{s}_{\gamma}}{\tau^{s}_{0}} \right)^{n^s} = \dot{\gamma\gamma}_0 \left(\frac{r^{s}_{ij} s_{ij}}{\tau^{s}_{0}} \right)^{n^s}, \qquad (7)$$

where $\dot{\gamma\gamma}_0$ is a reference strain rate, taken as 1 s^{-1}, and n^s, τ^s_γ and τ^s_0 are respectively the stress exponent, the resolved shear stress and the critical resolved shear stress for the system s, whose orientation relative to the macroscopic reference frame is expressed by its Schmid tensor $\mathbf{r}^s$. The total deformation rate is a linear combination of slip on all active slip systems. Crystal reorientation, and hence development of crystal preferred orientation, results from the discrepancy between the imposed macroscopic rotation rate and the spin associated with intracrystalline slip.

Except for computationally expensive n-site approaches, in which first-neighbour interactions are explicitly considered (Canova *et al.*, 1992; Wenk *et al.*, 1991), polycrystal plasticity models do not include a description of the microstructure. The interactions between a grain and its surroundings are described in a statistical way, by averaging the behaviour of individual grains using simple physically based assumptions. Classical lower- or upper-bound approaches impose homogeneous stress (Sachs, 1928) or strain (Taylor, 1938), respectively, within the aggregate. The Taylor assumption is reasonable for materials composed of crystals of a large number of slip systems with comparable strength. However, this is not the case for most mantle minerals like olivine, which displays less than five independent slip systems with very different strengths,

leading to significant variations in strain rate between differently oriented grains. The homogeneous stress model better represents the mechanical behaviour of these materials. However, in this model, deformation tends to be concentrated in a too small number of grains, leading to an underestimation of the mechanical strength and less accurate CPO predictions.

CPO in mantle minerals is better simulated by the viscoplastic self-consistent (VPSC) approach, initially developed by Molinari *et al.* (1987) and later generalised to anisotropic media by Lebensohn & Tomé (1993), which allows both the microscopic stress and strain rate (σ, $\dot{\varepsilon}$) to differ from the corresponding macroscopic quantities ($\bar{\Sigma}$, $\bar{D}$). Strain compatibility and stress equilibrium are ensured only at the aggregate scale. The problem lies in the calculation of a microscopic stress–strain rate state (σ, $\dot{\varepsilon}$) for each grain, whose volume average determines the mechanical response of the polycrystal. In the "1-site" approximation used in the anisotropic VPSC formulation (Lebensohn & Tomé, 1993), interactions between each grain and its surroundings are replaced by the interaction between an inclusion with the same lattice orientation and an infinite homogeneous equivalent medium (HEM), whose behaviour is the volume-weighted average of the grains' behaviour. This leads to:

$$\dot{\varepsilon}_{ij} - D_{ij} = -\alpha M_{ijkl}(\sigma_{kl} - \Sigma_{kl}), \tag{8}$$

where $\tilde{\mathbf{M}}$ is the interaction tensor and α is a constant used to parameterize the interaction between grains and the HEM. α = 0 corresponds to the upper-bound model (homogeneous strain), α = 1 is the tangent self-consistent model (linear relationship between volume-averaged stress and strain rate), and α = infinity corresponds to the lower-bound model (stress equilibrium). Extensive testing on metallic alloys (Lebensohn & Tomé, 1993; Logé *et al.*, 2000), halite (Lebensohn *et al.*, 2003), as well as on highly anisotropic minerals such as calcite (Tomé *et al.*, 1991), olivine (Tommasi *et al.*, 2000; Wenk *et al.*, 1991) and clinopyroxene (Bascou *et al.*, 2002), shows that the VPSC model produces robust CPO predictions. The effect of dynamic recrystallisation on CPO evolution may be integrated in polycrystal plasticity models through nucleation and growth criteria, which relate the evolution of the volume of each crystallographic orientation to the local strain rate, *i.e.*, to its Taylor factor (Kaminski & Ribe, 2001; Wenk *et al.*, 1997; Wenk & Tomé, 1999).

CPO evolution in this model is essentially controlled by the imposed deformation (or stress), the initial texture (crystal preferred and, to a lesser extent, shape preferred orientation) and the active slip systems. The latter depend on the mineral structure, but also on the temperature and pressure conditions, which control their relative strength or critical resolved shear stress (CRSS). The effect of the imposed deformation geometry on the CPO evolution may be illustrated by a series of simulations for olivine polycrystals (Fig. 15). These simulations show that the CPO symmetry results from an interplay of the crystal structure (symmetry and available slip systems) and the imposed deformation.

Comparison of simulation of CPO development in olivine polycrystals deformed under moderate and high-pressure conditions highlights the effect of a variation of the critical resolved shear stresses on the CPO evolution. Olivine deforms essentially by

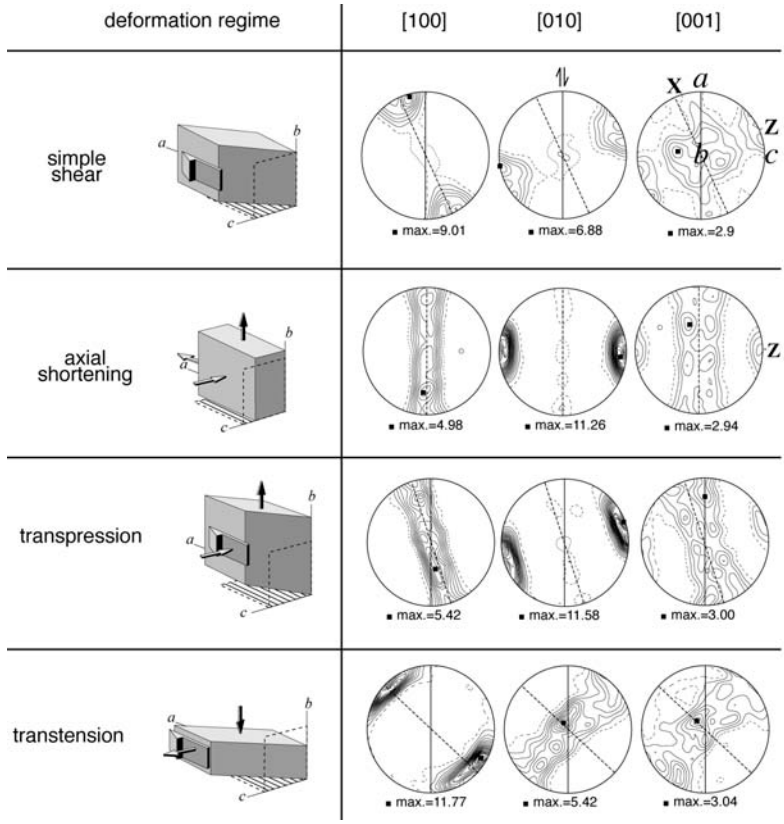

Fig. 15. Modelled CPO for olivine aggregates submitted to dextral simple shear, axial compression, transpression and transtension at an equivalent strain of 1. Equal area projections, lower hemisphere, 1000 grains, contours at multiples of a uniform distribution (mud) intervals. The shear plane (*ab* plane) and the foliation (XY plane) are represented by full and dashed lines, respectively. *a* is the shear direction and X the lineation (maximum stretching direction).

slip on [100]{0kl} and [001]{hk0} systems, mainly [100](010), [100](001), [001](010), [001](100), and [001]{110}. Experimental data as well as analysis of CPO in naturally-deformed mantle peridotites suggest that under high temperature–moderate pressure conditions, like those prevailing in the upper 200–250 km of the mantle, [100] slip is dominant. However, *ab initio* calculation presented above, in agreement with recent high-pressure experimental data of Couvy *et al.* (2004) suggest that [001] slip becomes predominant at high pressures. This transition has a drastic effect on the CPO evolution (Fig. 16). Simulations of a simple shear flow using low-pressure slip systems data show strong CPO characterised by progressive alignment of [100] with the shear direction and of [010] normal to the shear plane. In contrast, simulations using high-pressure data display very weak CPO in which [100] tends to orient normal to the lineation. The low-pressure simulated CPOs are in good agreement with those observed in high-temperature low-pressure simple shear

experiments on olivine polycrystals (Bystricky *et al.*, 2000; Zhang & Karato, 1995). They also correspond to the most commonly observed olivine CPO in naturally-deformed mantle xenoliths and peridotite massifs (Tommasi *et al.*, 2000). High-pressure simulations, on the other hand, reproduce the olivine CPO developed in simple shear experiments at 11 GPa (Couvy *et al.*, 2004).

Recent very high *P–T* deformation experiments designed to simulate transition zone and lower-mantle conditions have provided deformed crystals for the characterisation of the slip systems of the major mineral phases at these depths using conventional transmission electron microscopy (CTEM) and large-angle convergent beam electron diffraction (LACBED) (Cordier & Rubie, 2001; Couvy *et al.*, 2004; Thurel *et al.*, 2003a; Thurel *et al.*, 2003b). Based on these data, viscoplastic self-consistent models may now be used to predict CPO evolution as a response to flow in the transition zone (Tommasi *et al.*, 2004) and the lower mantle.

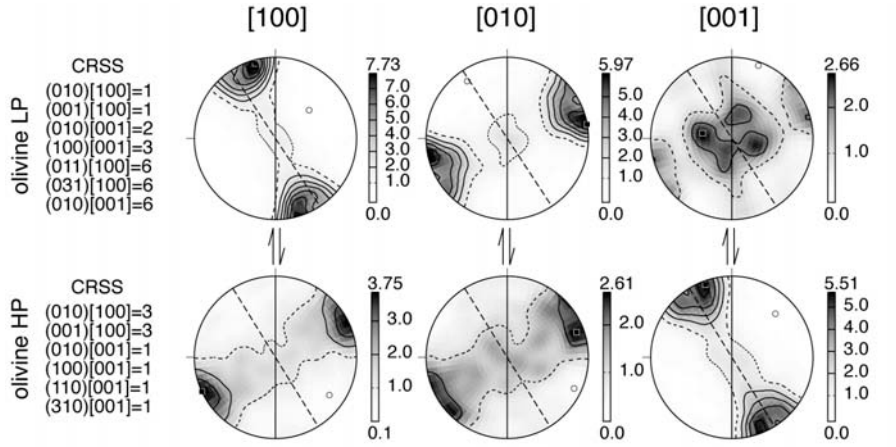

Fig. 16. Modelled CPO for olivine aggregates submitted to a dextral simple shear of 1 using critical resolved shear stresses representative of deformation at moderate- and high-pressure conditions. Equal area projections, lower hemisphere, 1000 grains, contours at multiples of an uniform distribution (mud) intervals. The shear plane and the foliation are represented by full and dashed lines, respectively.

Modelling polycrystal plasticity by finite elements

Among the different multiscale approaches that exist for the determination of the plasticity of heterogeneous materials, Finite Elements (FE) analysis has provided new insights since the 1990s (see for example Becker, 1991; Kalidindi *et al.*, 1992, Havlicek *et al.*, 1992; Beaudoin *et al.*, 1993). This approach applies crystalline plasticity constitutive laws at the scale of the crystals constituting the polycrystalline volume of study. A grain may be modelled as a single cubic element in the simplest representations of polycrystals. It may also be a set of elements, with the possibility to represent more complex grain morphologies, as in the example presented in this chapter. FE modelling allows prediction of effective properties of polycrystals and texture evolution. It shows also that stress and strain fields within a given grain are greatly influenced by interactions with its neighbours. This has enlightened the main breakthrough of FE:

providing information on the mechanical response of grains to the interaction with a heterogeneous medium rather than with a homogeneous one (as in the classical 1-site self-consistent schemes of homogenisation).

Since these pioneering works, an important progress has been made in the FE discretisation of crystals: first computations calling upon a discretisation of the grain interior were concerned with single or bicrystals (see for example Meric *et al.*, 1991), then with multicrystals (Teodosiu *et al.*, 1991; Raabe *et al.*, 2001), and finally, with realistic three-dimensional polycrystals (Quilici & Cailletaud 1999; Barbe *et al.*, 2001a, 2001b, 2003; Diard *et al.*, 2005). By realistic we mean that (i) the grains have realistic morphologies (see Fig. 17a) that differ from one to the other (this is achieved through the construction of Voronoi polyhedra[3]), (ii) a large enough number of elements is featured inside grains so that the local (intragranular) fields are independent on the choice of the discretisation, and (iii) a large enough number of grains is considered which ensures that one has a *poly*-crystal "in hand", or eventually a Representative Volume Element of a polycrystal.

A major difficulty for computing realistic 3D polycrystals comes from the huge amount of degrees of freedom in the mesh. The computation then requires large computer resources such as parallel computers. The computations presented here have been performed with the FE code ZeBuLoN (Ecole des Mines de Paris, ONERA; for characteristics, see for example Besson & Foerch, 1998, and Feyel, 1998), on 16 CPUs of a Linux cluster.

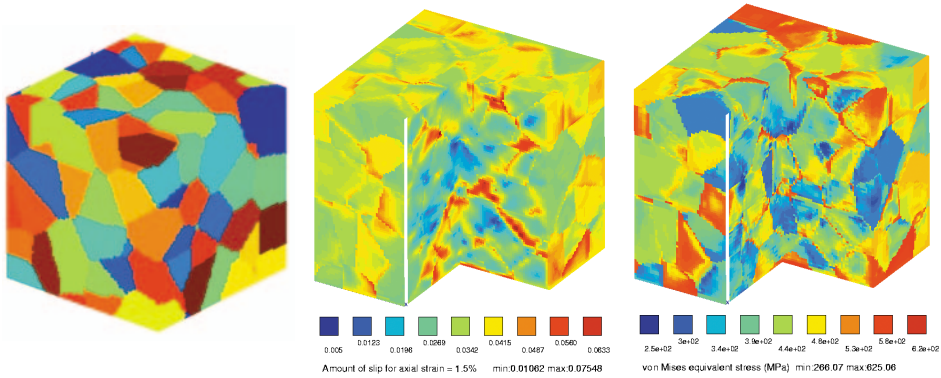

Fig. 17. (a) Polycrystalline aggregate made of 200 grains with morphologies of Voronoi polyhedra represented by 32^3 20-node brick elements. ***(b)*** Amount of plastic slip and ***(c)*** von Mises equivalent stress on the contour of the INCO600 polycrystal loaded at 1.5% axial strain with homogeneous strain boundary conditions (the mesh has been cut *a posteriori* in order to have a view on a part of the outer contour and inside the polycrystal).

For the modelling detailed here, the constitutive laws for single crystals assume that plastic deformation results from intragranular slip: slip rate is deduced with a viscoplastic law (as in Eqn. 7) from the resolved shear stress and the hardening contributions

[3] Given a set of points – the nuclei – randomly distributed in a three-dimensional space. With the Voronoi tesselation, the medium is divided into convex polyhedra, each one being defined as the set of points closest to the nucleus – the center – of the polyhedron than to any other nucleus. A polyhedron is thus the zone of influence of its nucleus, as crystals having grown simultaneously and at a same rate from randomly distributed nuclei.

(isotropic and kinematic hardening); then stress and strain tensors are determined according to the crystallographic orientation through the Schmid tensor. These constitutive laws are applied to each integration point of the FE mesh representing the polycrystal, such that each grain is made of a set of integration points. It is also possible to use Cosserat single-crystal plasticity, which takes into account non-local interactions at a given distance, such that grain size effects in polycrystals can be studied, as in Forest *et al.* (2000). As a first illustration of the results, Figures 17b and c present the contours of the amount of plastic slip and of von Mises equivalent stress after 1.5% axial strain prescribed to the 200-grain polycrystal with an isotropic texture of Figure 17a. The mesh is made of 32×32×32 20-node bricks and has been cut *a posteriori* in order to have a view on a part of the outer contour *and* inside the polycrystal. The material used for this illustration is INCO600, a nickel-based alloy with fcc structure. One may notice that even though von Mises stress seems strongly related to crystallographic orientations (it looks nearly homogeneous inside grains, with stress accommodation often taking place near grain boundaries), it is not the case for the amount of slip (and subsequently strains) which localises in regions crossing over few grains. This indicates that the range of strain interaction in polycrystals can be 2 or 3 times the mean size of grain.

Effective properties at the macroscopic scale

A first check of the validity of FE computations can be made by comparison with the prediction of a 1-site homogenisation model. Here, the self-consistent modelling of Berveiller & Zaoui (1979) has been used; it is characterised by the non-linear evolution of the interaction coefficient α of Equation 8 with the equivalent plastic strain and the overall equivalent stress.

Two extreme types of boundary conditions may be applied to the outer contour of the mesh; they lead respectively to the upper and lower bounds of the apparent properties of the polycrystal:

– homogeneous strain boundary conditions corresponding to a prescribed mean deformation tensor **E** of the aggregate. All components of the displacement vector **u** at each node (position x) of the outer boundary of the cube are prescribed according to: $\mathbf{u} = \mathbf{E}x$. The mean stress is deduced afterwards by volume averaging over the aggregate.

– homogeneous stress boundary conditions corresponding to a prescribed mean stress of the aggregate. The mean strain is deduced afterwards by volume averaging over the aggregate.

Other types of boundary conditions are mixed cases, with stress imposed on one part, strains or displacements on another part. It is of course possible to superimpose a hydrostatic pressure component at this stage. On Figure 18a, the mean stress–strain curves obtained by homogenisation and by FE with two extreme types of boundary conditions are compared. Whatever the boundary conditions, homogenisation and FE make very similar predictions. It is also shown that the mean properties are not significantly affected by the type of boundary conditions. These are two of the necessary conditions showing that the polycrystal is large enough and disordered enough to be considered as a Representative Volume Element, a volume whose mean (apparent) properties are representative of the macroscopic (effective) medium.

Scale of the mean behaviour of the grains

Homogenisation has in common with FE modelling the fact that it takes into account the heterogeneities at the scale directly smaller to the macroscopic scale, the scale of the grains. In 1-site homogenisation models, a grain is distinguished from another by its crystallographic orientation and by its volume only. In order to estimate the heterogeneity at this scale, the curves of the mean responses of all the grains of the polycrystal are presented on Figure 18b–c. Homogenisation results (Fig. 18b) are remarkable because of their location along a straight line at a given imposed strain. This is a direct consequence of the assumption that a grain interacts with a homogeneous medium. As seen with stress–strain curves of the FE computation and with the distributions of stress presented in the insets, the real neighbouring of a grain plays a major role in the behaviour of most of the grains, and tends to promote dispersion (Fig. 18c).

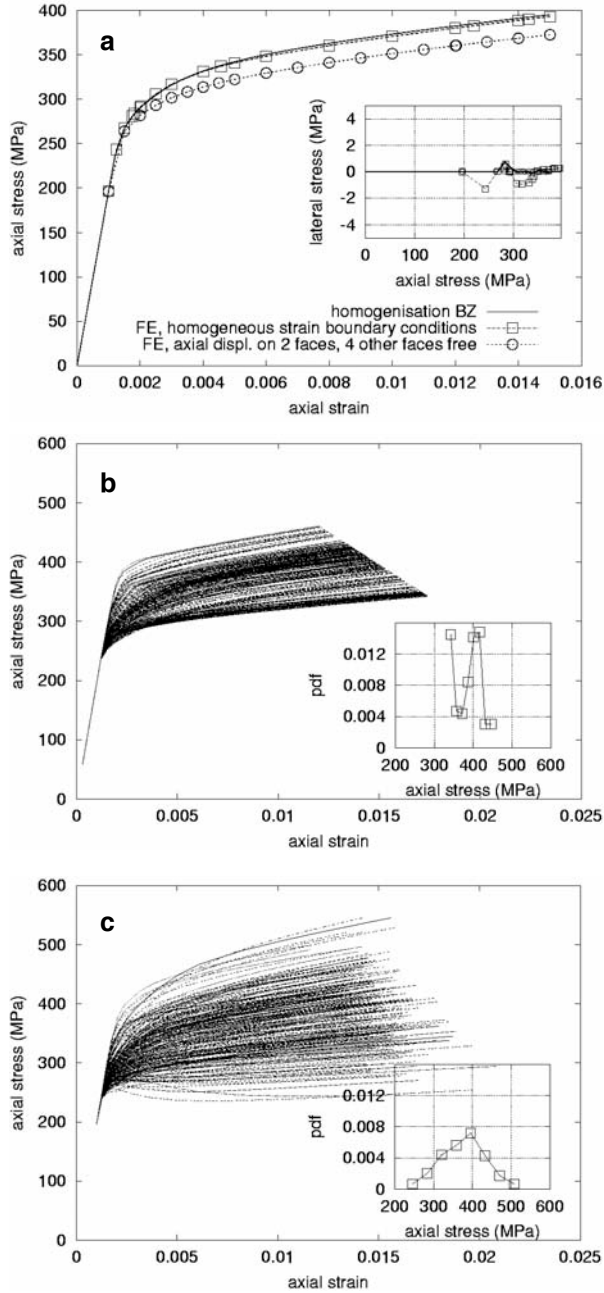

Fig. 18. (a) Effective response of the polycrystal subjected to a tensile test, from homogenisation and FE computations with two different boundary conditions; the inset shows the evolution of one of the principal stresses in a direction perpendicular to tension. ***(b)*** Mean response per grain according to homogenisation. ***(c)*** Mean response per grain according to FE with homogeneous strain boundary conditions; the insets show the distribution of the final axial stress in terms of estimation probability density function (pdf).

Intragranular scale

FE modelling also highlights the heterogeneities that develop inside the grains. This has been displayed qualitatively on Figure 17b and c and is confirmed here quantitatively on Figure 19a and b. Figure 19a presents the local responses of every integration point inside a given grain at three instants of the loading, while Figure 19b presents the local responses of all the integration points of the polycrystal at the end of loading. In both cases, the responses appear to be at least as dispersed as the mean responses per grain, as seen with the distributions in the insets. Another remark concerns the von Mises equivalent stress: contrary to any other variable (*e.g.* axial stress, strains), it has a non-symmetric distribution (this has been confirmed with computations on other polycrystals

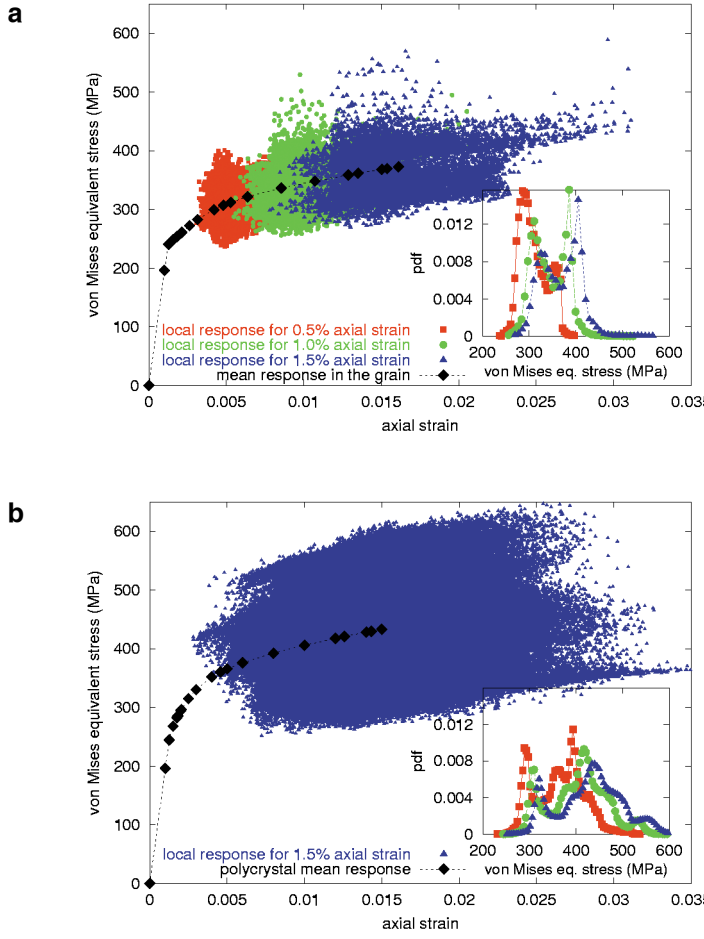

Fig. 19. (a) Mean stress–strain curve in a grain and local responses of every integration point of the grain at three instants of the loading. ***(b)*** Mean stress–strain curve in the polycrystal and local response of every integration point of the polycrystal at the end of the loading. Insets show the distribution of von Mises equivalent stress in terms of estimations of probability density functions.

of the same material), a peculiarity that is of importance for the validity of statistical approaches based on Gaussian distributions of equivalent stress. Only FE computations on polycrystals with realistic microstructures and fine enough discretisation of grains could allow this observation.

Case of a two-phase aggregate

Another potential application of FE modelling is the case of multi-phase materials, taking the actual morphology into account. As an illustration, Figure 20a presents the

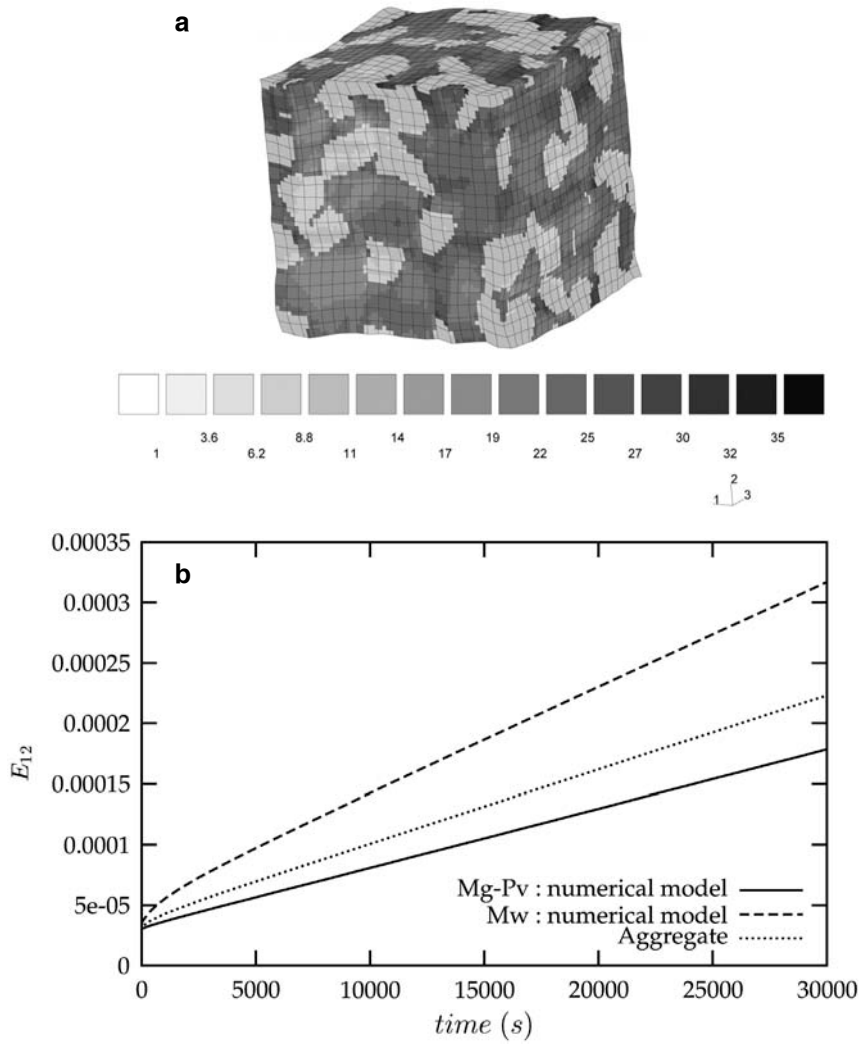

Fig. 20. FE modelling of a "70% hard/30% weak" two-phase aggregate (courtesy of K. Madi). ***(a)*** Contour of von Mises equivalent stress during steady-state creep under an applied shear stress of 10 MPa. ***(b)*** Macroscopic shear and average shear in the phases *versus* time.

case of a two-phase aggregate. This model experiment (Madi *et al.*, in press) is aimed at addressing the mechanical behaviour of a hypothetical lower-mantle assemblage containing 70% (volume fraction) of a hard phase (Mg,Fe perovskite) and 30% of a weak phase (magnesiowustite). In this simple experiment, an isotropic random polycrystal has been built from a Voronoi mosaic. Then each grain has been attributed a "hard" or "weak" behaviour. More complicated situations with the two phases having different mean grain sizes of spatial distribution within the volume could be considered. The creep law introduced for both phases is a simple Norton law without hardening. A contrast of 35 is chosen between the strain rates of both phases under a shear stress of 10 MPa. A representative volume element of 470 grains has been shown to provide a satisfactory description of the mechanical response of the aggregate (with 3% accuracy). Numerical creep experiments conducted under constant macroscopic shear stress of 10 MPa suggest that the creep rate of such a lower-mantle assemblage would be dominated by the mechanical behaviour of the perovskite phase. The finite element model allows to extract the individual behaviour of the two phases within the aggregate. It is shown that during creep the perovskite (hard) phase carries most of the stress whereas the magnesiowustite phase is responsible for most of the accumulated strain (Figure 20b).

FE modelling of polycrystals thus provides a powerful tool to predict material properties at different scales, from the intragranular scale (where the stress and strain fields inside the grain and the interactions with neighbouring grains are taken into account), to the macroscopic (or effective) scale of a polycrystal. It has been extensively used on different polycrystals of different crystalline viscoplastic materials and has always featured strong heterogeneities between grains as well as between points inside a same grain or inside the whole polycrystal. However, this approach requires the use of large-scale computing facilities and is therefore not recommended if one is only interested in investigations at the macroscopic scale: in this case, homogenisation would be more appropriate. An important improvement of these two types of modelling of polycrystals –homogenisation and FE – can be made by introducing more physically based constitutive laws and/or by resorting to the mechanics of generalised continua (Forest & Sedlacek, 2003).

Concluding remarks

Although we are just at the beginning of the development of multiscale modelling of the deformation of polycrystalline materials, we see that a wide range of powerful techniques is now becoming available. This brief overview also shows that multiscale modelling is also "multiphysics" as its background spans from quantum mechanics to continuum mechanics. This is what makes multiscale modelling unique for predicting the behaviour of materials under extreme pressure. As illustrated in the case of olivine, pressure can affect deformation mechanisms at the microscopic scale. It is only by taking these effects into account on a physical basis that one can imagine extrapolating their implications on the rheology of the deep Earth's materials. One of the major issue is thus to bridge length scales. This can be done by transferring features all the way up to the scale of realistic

materials. Another approach is to develop hybrid methods, for instance linking atomistic and continuum. Despite some promising attempts, the idea of describing macroscopic complex materials directly from first principles is still a vision of the future.

References

Barbe, F., Decker, L., Jeulin, D. & Cailletaud, G. (2001a): Intergranular and intragranular behavior of polycrystalline aggregates. Part 1: F.E. model. *Int. J. Plast.*, **17**:513–536.

Barbe, F., Forest, S. & Cailletaud, G. (2001b): Intergranular and intragranular behavior of polycrystalline aggregates. Part 2: results. *Int. J. Plast.*, **17**:537–563.

Barbe, F., Quilici, S., Forest, S. & Cailletaud, G. (2003): Numerical study of crystalline plasticity: measurements of the heterogeneities due to grain boundaries under small strains. *Rev. Métall.*, Septembre:815–823.

Bascou, J., Tommasi, A. & Mainprice, D. (2002): Plastic deformation and development of clinopyroxene lattice preferred orientations in eclogites. *J. Struct. Geol.*, **24**:1357–1368.

Beaudoin, A., Mathur, K., Dawson, P.R. & Johnson, G. (1993): Three-dimensional deformation process simulation with explicit use of polycrystal plasticity models. *Int. J. Plast.*, **9**:833–860.

Becker, R. (1991): Analysis of texture evolution in channel die compression. Effect of grain interaction. *Acta Metall. Mater.*, **39**:1211–1230.

Berveiller, M. & Zaoui, A. (1979): An extension of the self-consistent scheme to plastically flowing polycrystals. *J. Mech. Phys. Solids*, **26**:325–344.

Besson, J. & Foerch, R. (1998): Object-oriented programming applied to the finite element method. Part I. General concepts. *Rev. Eur. Elém. Finis*, **7**:535–566.

Bigger, J.R.K., McInnes, D.A., Sutton, A.P., Payne, M.C., Stich, I., King-Smith, R.D., Bird, D.M. & Clark, L.J. (1992): Atomic and electronic structures of the 90° partial dislocation in silicon. *Phys. Rev. Lett.*, **69**:2224–2227.

Braithwaite, J.S., Wright, K. & Catlow, C.R.A. (2003): A theoretical study of the energetics and IR frequencies of hydroxyl defects in forsterite. *J. Geophys. Res.*, **108**:2284.

Brodholt, J. (1997): Ab initio calculations on point defects in forsterite (Mg_2SiO_4) and implications for diffusion and creep. *Am. Mineral.*, **82**:1049–1053.

Bystricky, M., Kunze, K., Burlini, L. & Burg, J.P. (2000): High shear strain of olivine aggregates: Rheological and seismic consequences. *Science*, **290**:1564–1567.

Cai, W., Bulatov, V.V., Chang, J., Li, J. & Yip, S. (2001): Anisotropic elastic interactions of a periodic dislocation array. *Phys. Rev. Lett.*, **86**:5727–5730.

Canova, G.R., Wenk, H.-R. & Molinari, A. (1992): Deformation modelling of multi-phase polycrystals: case of a quartz-mica aggregate. *Acta Metall. Mater.*, **40**:1519–1530.

Cordier, P. & Rubie, D.C. (2001): Plastic deformation of minerals under extreme pressure using a multi-anvil apparatus. *Mater. Sci. Eng. A Struct. Mater.*, **309**:38–43.

Couvy, H., Frost, D., Heidelbach, F., Nyilas, K., Ungár, T., Mackwell, S. & Cordier, P. (2004): Shear deformation experiments of forsterite at 11 GPa – 1400 °C in the multianvil apparatus. *Eur. J. Mineral.*, **16**:877–889.

Craig, M.S., Warren, M.C., Dove, M.T., Gale, J.D., Sanchez-Portel, D., Ordejón, P., Soler, J.M. & Artacho, E. (2004): Simulations of minerals using density-functional theory based on atomic orbitals for linear scaling. *Phys. Chem. Miner.*, **31**:12–21.

Darot, M. & Gueguen, Y. (1981): High-temperature creep of forsterite single crystals. *J. Geophys. Res.*, **86**:6219–6234.

de Leeuw, N.H., Parker, S.C., Catlow, C.R.A. & Price, G.D. (2000): Proton-containing defects at forsterite {010} tilt grain boundaries and stepped surfaces. *Am. Mineral.*, **85**:1143–1154.

Devincre, B. & Condat, M. (1992): Discretization and line tension effects. *Acta Metall. Mater.*, **40**:2629–2637.

Devincre, B., Kubin, L.P., Lemarchand, C. & Madec, R. (2001): Mesoscopic simulations of plastic deformation. *Mater. Sci. Eng. A, Struct. Mater.*, **309**:211–219.

Diard, O., Leclercq, S., Rousselier, G. & Cailletaud, G. (2005): Evaluation of finite element based analysis of 3D multicrystalline aggregates plasticity: Application to crystal plasticity model identification and the study of stress and strain fields near grain boundaries. *Int. J. Plast.*, **21**:694–722.

Durham, W.B., Goetze, C. & Blake, B. (1977): Plastic flow of oriented single crystals of olivine. 2. Observations and interpretations of the dislocation structures. *J. Geophys. Res.*, **82**:5755–5770.

Evans, B. & Goetze, C. (1979): The temperature variation of hardness in olivine and its implication for polycrystalline yield stress. *J. Geophys. Res.*, **84**:5505–5524.

Feyel, F. (1998): *Application du calcul parallèle aux modèles à grand nombre de variables internes*. PhD Thesis. Paris: Ecole Nationale Supérieure des Mines.

Forest, S., Barbe, F. & Cailletaud, G. (2000): Cosserat modelling of size effects in the mechanical behaviour of polycrystals and multiphase materials. *Int. J. Solids Struct.*, **37**:7105–7126.

Forest, S. & Sedlacek, R. (2003): Plastic slip distribution in two-phase laminate microstructures: Dislocation-based vs. generalized-continuum approaches. *Philos. Mag*, **83**:245–276.

Gaboriaud, R.J. (1986): Dislocations in olivine single crystals indented between 25 and 1100°C. *Bull. Minéral.*, **109**:185–191.

Gaboriaud, R.J., Darot, M., Gueguen, Y. & Woigard, J. (1981): Dislocations in olivine indented at low temperatures. *Phys. Chem. Miner.*, **7**:100–104.

Gale, J.D. & Rohl, A.L. (2003): The General Utility Lattice Program (GULP). *Mol. Simul.*, **29**:291–341.

Gehlen, P.C., Hirth, J.P., Hoagland, R.G. & Kanninen, M.F. (1972): A new representation of the strain field associated with the cube-edge dislocation of α-iron. *J. Appl. Phys.*, **43**:3921–3933.

Gueguen, Y. & Darot, M. (1982): Les dislocations dans la forsterite déformée à haute température. *Philos. Mag. A*, **45**:419–442.

Havlicek, F., Tokuda, M., Hino, S. & Kratochvil, J. (1992): Finite element method analysis of micro-macro transition in polycrystalline plasticity. *Int. J. Plast.*, **8**:477–499.

Hoagland, R.G., Hirth, J.P. & Gehlen, P.C. (1976): Atomic simulation of the dislocation core structure and Peierls stress in alkali halide. *Philos. Mag.*, **34**:413–439.

Kalidindi, S., Bronkhorst, C. & Anand, L. (1992): Crystallographic evolution in bulk deformation processing of FCC metals. *J. Mech. Phys. Solids*, **40**:537–569.

Kaminski, E. & Ribe, N.M. (2001): A kinematic model for recrystallization and texture development in olivine polycrystals. *Earth Planet. Sci. Lett.*, **189**:253–267.

Kocks, U.F., Argon, A.S. & Ashby, M.F. (1975): *Thermodynimics and kinetics of slip*. Oxford: Pergamon Press.

Kresse, G. & Furthmüller, J. (1996a): Efficiency of ab-initio total energy calculations for metals and semiconductors using a plane-wave basis set. *Comput. Mater. Sci.*, **6**:15–50.

Kresse, G. & Furthmüller, J. (1996b): Efficient iterative schemes for ab initio total-energy calculations using a plane-wave basis set. *Phys. Rev. B*, **54**:11169.

Kresse, G. & Hafner, J. (1993): Ab initio molecular dynamics for liquid metals. *Phys. Rev. B*, **47**:558.

Lebensohn, R.A. & Tomé, C.N. (1993): A self-consistent anisotropic approach for the simulation of plastic deformation and texture development of polycrystal: application to zirconium alloys. *Acta Metall. Mater.*, **41**:2611–2624.

Lebensohn, R.A., Dawson, P.R., Kern, H.M. & Wenk, H.R. (2003): Heterogeneous deformation and texture development in halite polycrystals: comparison of different modeling approaches and experimental data. *Tectonophysics*, **370**:287–311.

Logé, R.E., Signorelli, J.W., Chastel, Y.B., Perrin, M.Y. & Lebensohn, R.A. (2000): Sensitivity of alpha-Zy4 high-temperature deformation textures to beta-quenched precipitate structure and to recrystallization: application to hot extrusion. *Acta Mater.*, **48**:3917–3930.

Madec, R., Devincre, B. & Kubin, L.P. (2001): New line model for optimized dislocation dynamics simulations. *Mater. Res. Symp. Proc*., **653**:Z1.8.1–6.

Madec, R., Devincre, B. & Kubin, L.P. (in press): On the use of periodic boundary conditions in dislocation dynamics simulation. *In* Shibutani, Y. & Kitagawa, H. (eds.): *Mesoscopic dynamics in fracture process and strength of materials*. Dordrecht: Kluwer.

Madi, K., Forest, S., Cordier, P. & Boussuge, M. (in press): Numerical study of creep in two-phase aggregates with a large rheology contrast: implications for the lower mantle. *Earth Planet. Sci. Lett.*

Marian, J., Cai, W. & Bulatov, V.V. (2004): Dynamic transitions from smooth to rough to twinning in dislocation motion. *Nat. Mater.*, **3**:158–163.

Martsinovich, N., Heggie, M.I. & Ewels, C.P. (2003): First-principles calculations on the structure of hydrogen aggregates in silicon and diamond. *J. Phys., Condens. Mater.*, **15**:S2815–S2824.

Méric, L., Poubanne, P. & Cailletaud, G. (1991): Single crystal modeling for structural calculations. Part 1: Model presentation. *J. Eng. Mater. Technol.*, **113**:162–170.

Molinari, A., Canova, G.R. & Azhy, S. (1987): A self-consistent approach of the large deformation crystal polycrystal viscoplasticity. *Acta Metall.*, **35**:2983–2994.

Monnet, G., Devincre, B. & Kubin, L.P. (2004): Dislocation study of prismatic slip systems and their interactions in hexagonal close packed metals: application to zirconium. *Acta Mater.*, **52**:4317–4328.

Phakey, P., Dollinger, G. & Christie, J.M. (1972): Transmission Electron Microscopy of experimentally deformed olivine crystals. *In* Heard, H.C. *et al.* (eds.): *Flow and fracture of rocks /Geophys. Monogr. Ser*., **16**/. Washington (D.C.): Am. Geophys. Union, 139–156.

Puls, M.P. & Norgett, M.J. (1976): Atomistic calculation of the core structure and Peierls energy of an (a/2)[110] edge dislocation in MgO. *J. Appl. Phys.*, **47**:466–477.

Quilici, S. & Cailletaud, G. (1999): F.E. simulation of macro-, meso- and micro-scales in polycrystalline plasticity. *Comput. Mater. Sci.*, **16**:383–390.

Raabe, D., Sachtleber, M., Zhao, Z., Roters, F. & Zaefferer, S. (2001): Micromechanical and macromechanical effects in grain scale polycrystal plasticity – experimentation and simulation. *Acta Mater.*, **49**:3433–3441.

Rao, S., Hernandez, D., Simmond, J.P., Parthasarathy, T.A. & Woodward, C. (1998): Green's function boundary conditions in two-dimensional and three-dimensional atomistic simulations of dislocations. *Philos. Mag. A*, **77**:231–256.

Sachs, G. (1928): Zur Ableitung einer Fliessbedingung. *Z. Ver. Dtsch. Ing.*, **72**:734–736.

Saunders, V.R., Freyria-Fava, C., Dovesi, R. & Roetti, C. (1994): On the electrostatic potential in linear periodic polymers. *Comput. Phys. Comm.*, **84**:156–172.

Sinclair, J.E., Gehlen, P.C., Hoagland, R.G. & Hirth, J.P. (1978): Flexible boundary conditions and nonlinear geometric effects in atomic dislocation modeling. *J. Appl. Phys.*, **49**:3890–3897.

Steeds, J.W. (1973): *Introduction to anisotropic elasticity theory of dislocations*. Oxford: Oxford Univ. Press, 274 p.

Tang, M., Kubin, L.P. & Canova, G. (1998): Dislocation mobility and the mechanical response of bcc crystals: a mesoscopic approach. *Acta Mater.*, **46**:3221–3235.

Taylor, G.I. (1938): Plastic strain in metals. *J. Inst. Metall.*, **62**:307–324.

Teodosiu, C., Raphanel, J. & Tabourot, L. (1991): Finite element simulation of the large elastoplastic deformation of multicrystals. *In* Teodosiu, C., Raphanel, J. & Sidoroff, F. (eds.): *Mecamat '91: Large plastic deformations, fundamental aspects and applications to metal forming. Fontainebleau, France*, 153–168.

Thurel, E., Cordier, P., Frost, D. & Karato, S. (2003a): Plastic deformation of wadsleyite: II. High-pressure deformation in shear. *Phys. Chem. Miner.*, **30**:267–270.

Thurel, E., Douin, J. & Cordier, P. (2003b): Plastic deformation of wadsleyite: III. Interpretation of dislocations and slip systems. *Phys. Chem. Miner.*, **30**:271–279.

Tomé, C.N., Wenk, H.-R., Canova, G. & Kocks, U.F. (1991): Simulations of texture development in calcite: comparison of polycrystal plasticity theories. *J. Geophys. Res.*, **96**:11865–11875.

Tommasi, A., Cordier, P., Mainprice, D., Couvy, H. & Thoraval, C. (2004): Strain-induced seismic anisotropy of wadsleyite polycrystal: constraints on flow patterns in the mantle transition zone. *J. Geophys. Res.*, **109**:B12405.

Tommasi, A., Mainprice, D., Canova, G. & Chastel, Y. (2000): Viscoplastic self-consistent and equilibrium-based modeling of olivine lattice preferred orientations: Implications for the upper mantle seismic anisotropy. *J. Geophys. Res.*, **105**:7893–7908.

Vitek, V. (1968): Intrinsic stacking faults in body-centered cubic crystals. *Philos. Mag. A*, **18**:773–786.

Walker, A.M., Wright, K. & Slater, B. (2003): A computational study of oxygen diffusion in olivine. *Phys. Chem. Mineral*., **30**: 536–545.

Walker, A.M., Slater, B., Gale, J.D. & Wright, K. (2004): Predicting the structure of screw dislocations in nanoporons materials. *Nat. Mater.*, **3**: 715–720.

Wang, Y., Liebermann, R.C. & Boland, J.N. (1988): Olivine as an in situ piezometer in high-pressure apparatus. *Phys. Chem. Miner.*, **15**:493–497

Watson, G.W., Kelsey, E.T. & Parker, S.C. (1999): Atomistic simulation of screw dislocations in rock salt structured materials. *Philos. Mag. A*, **79**:527–536.

Wenk, H.R. & Tomé, C.N. (1999): Modelling dynamic recrystallization of olivine aggregates deformed in simple shear. *J. Geophys. Res.*, **104**:25513–25527.

Wenk, H.-R., Bennett, K., Canova, G.R. & Molinari, A. (1991): Modelling plastic deformation of peridotite with the self-consistent theory. *J. Geophys. Res.*, **96**:8337–8349.

Wenk, H.-R., Canova, G., Brechet, Y. & Flandin, L. (1997): A deformation-based model for recrystallization of anisotropic materials. *Acta Metall. Mater.*, **45**:3283–3296.

Zbib, H.M., Rhee, M. & Hirth, J.P. (1998): On plastic deformation and the dynamics of 3D dislocations. *Int. J. Mech. Sci.*, **40**:113–127.

Zhang, S. & Karato, S. (1995): Lattice preferred orientation of olivine aggregates deformed in simple shear. *Nature*, **375**:774–777.